Available online at www.sciencedirect.com
ScienceDirect
Journal of Computational Physics 227 (2008) 5649–5670
JOURNAL OF COMPUTATIONAL PHYSICS
www.elsevier.com/locate/jcp

An explicit discontinuous Galerkin scheme with local time-stepping for general unsteady diffusion equations

Frieder Lörcher *, Gregor Gassner, Claus-Dieter Munz

Institut für Aerodynamik und Gasdynamik, Universität Stuttgart, Pfaffenwaldring 21, 70569 Stuttgart, Germany

Received 26 July 2007; received in revised form 23 October 2007; accepted 3 February 2008
Available online 26 February 2008

Abstract

In this paper we propose a discontinuous Galerkin scheme for the numerical approximation of unsteady heat conduction and diffusion problems in multi dimensions. The scheme is based on a discrete space–time variational formulation and uses an explicit approximative solution as predictor. This predictor is obtained by a Taylor expansion about the barycenter of each grid cell at the old time level in which all time or mixed space–time derivatives are replaced by space derivatives using the differential equation several times. The heat flux between adjacent grid cells is approximated by a local analytical solution. It takes into account that the approximate solution may be discontinuous at grid cell interfaces and allows the approximation of discontinuities in the heat conduction coefficient. The presented explicit scheme has to satisfy a typical parabolic stability restriction. The loss of efficiency, especially in the case of strongly varying sizes of cells in unstructured grids, is circumvented by allowing different time steps in each grid cell which are adopted to the local stability restrictions. We discuss the linear stability properties in this case of varying diffusion coefficients, varying space increments and local time steps and extent these considerations also to a modified symmetric interior penalization scheme. In numerical simulations we show the efficiency and the optimal order of convergence in space and time.

Keywords: Discontinuous Galerkin schemes; Nonlinear unsteady diffusion equations; High order accuracy; Space–time approach; Numerical flux for heat conduction; Local time-stepping

1. Introduction

The usual numerical approximation for the transient heat conduction equation are implicit finite difference and finite element schemes with second-order accuracy in space and time. Explicit schemes need less computational effort per time step, but have to satisfy a severe time step restriction for stability. The time step has to be proportional to the square of the diameter of the smallest grid cell. This restrictive time step limitation may

* Corresponding author. Tel.: +49 711 685 63407; fax: +49 711 685 63438.
E-mail addresses: loercher@iag.uni-stuttgart.de (F. Lörcher), gassner@iag.uni-stuttgart.de (G. Gassner), munz@iag.uni-stuttgart.de (C.-D. Munz).

0021-9991/$ - see front matter © 2008 Elsevier Inc. All rights reserved.
doi:10.1016/j.jcp.2008.02.015

strongly reduce the efficiency of the explicit approach, especially in the case of strongly varying grid cell sizes. In this paper, we propose an explicit discontinuous Galerkin scheme where the strong drop in efficiency is circumvented by local time-stepping. The scheme is designed such that every grid cell runs with its own time step as given by the local stability restriction – global time levels are no longer necessary. The scheme proposed is of arbitrary order of accuracy, both in space and time. As a discontinuous Galerkin finite element scheme it is applied to quite general unstructured grids, e.g., with hanging nodes. With these features the scheme seems to be ideal for highly unsteady problems on strongly varying spatial grids or for solutions with locally quite different behavior.

The discontinuous Galerkin (DG) finite element schemes scheme was originally proposed by Reed and Hill [17] in 1973 for the numerical solution of neutron transport and by Nitsche [16] in 1971 for the approximation of elliptic equations. The application to time dependent hyperbolic conservation laws was starting with the work of Cockburn and Shu [8]. For hyperbolic problems it turned out within the last decade that DG schemes are one of the most interesting candidates to construct high order schemes for complex geometries. This is due to the fact that in the DG approach the approximate solutions are allowed to be discontinuous at the grid cell interfaces. The numerical flux takes into account the discontinuity and uses information of the break up of these discontinuities into different waves. How to do this in a proper way has been shown within the development of the finite volume schemes. Even in the case of the approximation of strong local gradients on a coarse grid, this construction still leads to a consistent approximation, e.g., in terms of approximate values for the averages of the grid cells. By this, it is possible to establish a consistent and stable approximation of strong gradients and even the shock-capturing property. For a review of the development of DG methods see [7].

The definition of appropriate numerical fluxes for diffusion terms needed some additional work of research. The jumps of the approximate solution has to be taken into account in a proper way. This is more subtle for diffusion terms, because the flux involves derivatives of the solution. To take simply the arithmetic mean of the derivatives from the right and the left may be inconsistent for DG or FV schemes, because the influence of the jump is neglected. A number of corrections and better definitions of the diffusion fluxes has been proposed. A unified formulation and analysis for the stationary case has been given by Arnold et al. in [2] and was continued in [3].

In [10] we recently proposed for the unsteady one-dimensional case the use of the exact solution of the initial value problem with piecewise polynomial initial data to get an appropriate diffusion flux for finite volume and discontinuous Galerkin schemes. The flux of this local solution is defined to be the numerical flux at the grid cell interfaces. In combination with a variational formulation performing a second partial integration it was observed that this approach also recovers the symmetric interior penalty (SIP) discontinuous Galerkin scheme, already proposed in [16] for the approximation of elliptic equations, and gives a physical foundation of this method. In this paper, the so-called dGRP method (diffusive generalized Riemann problem) is extended and formulated in multi space dimensions on unstructured grids for general diffusion problems including discontinuous and nonlinear diffusion coefficients. The scheme allows the approximation of heat conduction problems across media where the thermal coefficient is discontinuous conforming to the grid. Due to the locality of this scheme we are able to introduce time-consistent local time-stepping which strongly increases the efficiency. We analyze the linear stability in case of a uniform grid and extent it to non-uniform grids with varying diffusion coefficients. The results obtained also show how to choose the penalization constants in order to maximize the time step within an explicit scheme based on a symmetric interior penalty spatial operator.

The format of this paper is as follows. In Section 2 we describe the DG scheme based on a space–time expansion (STE-DG) for a quite general heat conduction equation in multi dimensions. The dGRP flux between the grid cells is motivated by the solution of the diffusive generalized Riemann problem which is shortly surveyed. The dGRP method is then extended to handle jumps of the heat conduction coefficient at a material interface which is aligned with the grid. A description of the local time-stepping is included. Section 3 contains the matrix stability analysis and the implications for the choice of the optimal penalty parameter and time step. Numerical results for a number of test problems are given in Section 4. Section 5 contains our conclusions.

2. A discontinuous Galerkin scheme based on a space–time expansion

2.1. Governing equation

In this section, we consider a scalar heat conduction on a space–time domain $\Omega \times [0,T] \subset \mathbb{R}^d \times \mathbb{R}_0^+$ of the form

$$c(\vec{x},\theta)\theta_t - \vec{\nabla}\cdot(k(\vec{x},\theta)\vec{\nabla}\theta) = 0, \quad \text{for } (\vec{x},t) \in \Omega \times [0,T]. \tag{2.1}$$

The desired solution is a positive function $\theta = \theta(\vec{x},t)$ and represents the temperature. Further, c and k are given positive functions of $\vec{x}$ and θ.

If the primitive function of c with respect to θ:

$$u(\vec{x},\theta) = \int_{\theta_0}^{\theta} c(\vec{x},\theta)\mathrm{d}\theta \tag{2.2}$$

exists for each $\vec{x}$, then the Eq. (2.1) can also be written in the form

$$u_t - \vec{\nabla}\cdot\left(\frac{k(\vec{x},\theta(u))}{c(\vec{x},\theta(u))}\vec{\nabla}u\right) = 0. \tag{2.3}$$

Due to the positivity of c the mapping $u = u(\theta)$ is bijective. Eq. (2.3) represents the underlying physical principle of the conservation of the internal energy $u(\theta)$. With the definition

$$\mu(\vec{x},u) := \frac{k(\vec{x},\theta(u))}{c(\vec{x},\theta(u))} \tag{2.4}$$

Eq. (2.3) reads as

$$u_t - \vec{\nabla}\cdot(\mu\vec{\nabla}u) = 0. \tag{2.5}$$

In situations where discontinuities in the material properties $c(\vec{x},\theta)$ and $k(\vec{x},\theta)$ occur the conservative form is the better one, because it allows to switch to a weak or variational formulation of the equation and to look for weak solutions.

2.2. Weak formulation

For approximation the domain Ω is subdivided in non-overlapping spatial grid cells Q_i with surfaces ∂Q_i. To derive a weak formulation we first multiply Eq. (2.5) by a test function $\phi = \phi(\vec{x})$ and integrate over an arbitrary space–time cell $Q_i^n := Q_i \times [t^n, t^{n+1}]$:

$$\int_{Q_i^n} (u_t - \vec{\nabla}\cdot(\mu\vec{\nabla}u))\phi \,\mathrm{d}\vec{x}\,\mathrm{d}t = 0. \tag{2.6}$$

As usual in the finite element framework we apply integration by parts of the flux terms with respect to the space variables and obtain

$$\int_{Q_i^n} u_t\phi \,\mathrm{d}\vec{x}\,\mathrm{d}t - \int_{\partial Q_i^n} \mu\vec{\nabla}u\cdot\vec{n}\phi \,\mathrm{d}s\,\mathrm{d}t + \int_{Q_i^n} \mu\vec{\nabla}u\cdot\vec{\nabla}\phi \,\mathrm{d}\vec{x}\,\mathrm{d}t = 0, \tag{2.7}$$

where $\vec{n}$ denotes the normal vector into the outer direction of the side faces $\partial Q_i^n := \partial Q_i \times [t^n, t^{n+1}]$ of the space–time cell.

We proceed by applying a second integration by parts to the volume integral in (2.7) in order to take into account the second-order derivatives of the governing equation:

$$\begin{aligned} &\int_{Q_i^n} \mu\vec{\nabla}u\cdot\vec{\nabla}\phi \,\mathrm{d}\vec{x}\,\mathrm{d}t = \int_{Q_i^n} \vec{\nabla}u\cdot\mu\vec{\nabla}\phi \,\mathrm{d}\vec{x}\,\mathrm{d}t \\ &= \int_{\partial Q_i^n} u\mu\vec{\nabla}\phi\cdot\vec{n}\,\mathrm{d}s\,\mathrm{d}t - \int_{Q_i^n} u\vec{\nabla}\cdot(\mu\vec{\nabla}\phi)\mathrm{d}\vec{x}\,\mathrm{d}t, \end{aligned} \tag{2.8}$$

and end up with the weak formulation

$$\int_{Q_i^n} u_t \phi \,\mathrm{d}\vec{x}\,\mathrm{d}t + \int_{\partial Q_i^n} \mu(u\vec{\nabla}\phi \cdot \vec{n} - \vec{\nabla}u \cdot \vec{n}\phi)\mathrm{d}s\,\mathrm{d}t - \int_{Q_i^n} u\vec{\nabla} \cdot (\mu\vec{\nabla}\phi)\mathrm{d}\vec{x}\,\mathrm{d}t = 0. \tag{2.9}$$

2.3. The discrete variational formulation

We next define the approximate solution $u_h = u_h(\vec{x}, t)$ which is at each fixed time level a piecewise polynomial in space. In the grid cell Q_i it is represented by

$$u_i(\vec{x}, t) = \sum_{l=0}^{\mathcal{N}(N,d)} \hat{u}_{i,l}(t)\phi_{i,l}(\vec{x}), \tag{2.10}$$

where $\phi_{i,l} = \phi_{i,l}(\vec{x}), l = 1, \ldots, \mathcal{N}(N, d)$ are basis functions which span the space of polynomials of degree N with support Q_i, and $\hat{u}_{i,l}(t), l = 1, \ldots, \mathcal{N}(N, d)$, are the time dependent degrees of freedom (DOF). $\mathcal{N} = \mathcal{N}(N, d)$ is the number of DOF needed in d space dimensions in order to span a polynomial space of degree N. We use orthonormal basis functions which are constructed using the Gram–Schmidt orthogonalization algorithm yielding a diagonal mass matrix, even for elements with curved boundaries.

The temporal evolution of the degrees of freedom is represented by discrete values at the different time levels, e.g., at the time level t^n we have

$$u_i(\vec{x}, t^n) = \sum_{l=0}^{\mathcal{N}} \hat{u}_{i,l}(t^n)\phi_{i,l}(\vec{x}) =: \sum_{l=0}^{\mathcal{N}} \hat{u}_{i,l}^n \phi_{i,l}(\vec{x}). \tag{2.11}$$

We insert this approximate solution into the weak formulation (2.9) and choose the test functions equal to the basis functions $\phi_{i,l} = \phi_{i,l}(\vec{x}), l = 1, \ldots, \mathcal{N}(N, d)$. As the approximate solution u_i is discontinuous at element interfaces, we have to introduce numerical approximations for the fluxes $\vec{f} := \mu\vec{\nabla}u$ and $f^a := \mu u$ in the surface flux integrals, which we denote by $\vec{g}$ and g^a, respectively. The discrete weak formulation then reads as

$$\int_{Q_i^n} \frac{\partial}{\partial t} u_i \phi \,\mathrm{d}\vec{x}\,\mathrm{d}t + \int_{\partial Q_i^n} (g^a \vec{\nabla}\phi \cdot \vec{n} - \vec{g} \cdot \vec{n}\phi)\mathrm{d}s\,\mathrm{d}t - \int_{Q_i^n} u_i \vec{\nabla} \cdot (\mu\vec{\nabla}\phi)\mathrm{d}\vec{x}\,\mathrm{d}t = 0. \tag{2.12}$$

In the numerical approximation we assume that the surface flux terms cover the exchange across the interface and are determined by the approximate solution from both sides, while the volume integral is evaluated by interior values only. Using this information the volume integral term can then be evaluated more efficiently, if the reverse integration by parts is applied:

$$\int_{Q_i^n} u_i \vec{\nabla} \cdot (\mu\vec{\nabla}\phi)\mathrm{d}\vec{x}\,\mathrm{d}t = \int_{\partial Q_i^n} [u_i \mu\vec{\nabla}\phi \cdot \vec{n}]^- \mathrm{d}s\,\mathrm{d}t - \int_{Q_i^n} \mu\vec{\nabla}u_i \cdot \vec{\nabla}\phi \mathrm{d}\vec{x}\,\mathrm{d}t, \tag{2.13}$$

where $[.]^-$ means the evaluation of the function at the boundary of Q_i^n from the interior of the grid cell. Inserting this relation into the Eq. (2.12) yields the discrete variational formulation of Eq. (2.5) as

$$\int_{Q_i^n} \frac{\partial}{\partial t} u_i \phi \,\mathrm{d}\vec{x}\,\mathrm{d}t - \int_{\partial Q_i^n} \vec{g} \cdot \vec{n}\phi \,\mathrm{d}s\,\mathrm{d}t + \int_{Q_i^n} \mu\vec{\nabla}u_i \cdot \vec{\nabla}\phi \,\mathrm{d}\vec{x}\,\mathrm{d}t + \int_{\partial Q_i^n} g_{\vec{n}}^a \,\mathrm{d}s\,\mathrm{d}t = 0 \tag{2.14}$$

with

$$g_{\vec{n}}^a = g^a \vec{\nabla}\phi \cdot \vec{n} - [f^a \vec{\nabla}\phi \cdot \vec{n}]^-. \tag{2.15}$$

Here, we followed the variational formulation as introduced by Gassner et al. in [10]. The second partial integration generates a numerical surface flux $g_{\vec{n}}^a$ additional to $\vec{g}$ which gives adjoint consistency and is similar to the'symmetric term' in the Symmetric Interior Penalty (SIP) method as proposed by Hartmann and Houston [13] and the term of the BR2 scheme of Bassi and Rebay [5] involving the global lifting operator.

The temporal evolution of the DOF of an element Q_i for the time step $[t^n, t^{n+1}]$ is then given by

$$\hat{u}_i^{n+1} - \hat{u}_i^n = -\int_{Q_i^n} \mu \vec{\nabla} u_i \cdot \vec{\nabla}\phi \, \mathrm{d}\vec{x}\,\mathrm{d}t + \int_{\partial Q_i^n} \vec{g} \cdot \vec{n}\phi \, \mathrm{d}s\,\mathrm{d}t - \int_{\partial Q_i^n} g_{\vec{n}}^a \, \mathrm{d}s\,\mathrm{d}t. \tag{2.16}$$

The proper definition of these numerical flux functions guarantees stability and consistency of the approximation and is given in the following Section 2.4.

The space–time integrals in (2.16) are computed using Gaussian quadrature formulae in space and time. The accuracy of the Gauss quadrature rule in space is chosen in such a way that polynomials of degree $2N-1$ are integrated exactly, since the flux is multiplied by a test function which is a polynomial in space. For the quadrature rule in time we can use a formula that integrates exactly a polynomial of degree

$$\#\frac{N}{2} := \begin{cases} \frac{N}{2} & \text{for } N \text{ even}, \\ \frac{N+1}{2} & \text{for } N \text{ odd}, \end{cases} \tag{2.17}$$

as the test functions do not depend on the time variable and for stability restrictions we have to satisfy $\Delta t \sim \Delta x^2$ as usual for explicit schemes. We will come back to this point in Section 3.

How to evaluate the arguments of the numerical flux functions at space–time Gaussian points is still open, since the DOF $\hat{u}_i^n$ define the numerical solution only at $t = t^n$. This procedure is described in Section 2.5.

2.4. Numerical fluxes

For the approximation of the fluxes $\vec{g}$ and $g_{\vec{n}}^a$ into normal direction to a face of a grid cell, the rotational invariance of Eq. (2.5) is used. For every quadrature point on the element faces, the gradient of the state variable $\vec{\nabla} u$ is rotated from the global $\vec{x}$-system into the $\vec{\xi}$-system aligned with normal and tangential directions of the side surface. Here, the first component ξ_1 of the $\vec{\xi}$-system is aligned with the outward-pointing normal vector of the surface. The transformation can be written as

$$\vec{\nabla}_{\vec{\xi}} u = \underline{T} \nabla_{\vec{x}} u, \tag{2.18}$$

where the subscripts denote the gradients with respect to the corresponding coordinates.

Using the rotational invariance

$$\vec{f}(u, \vec{\nabla}_{\vec{x}} u) \cdot \vec{n} = f_1(u, \vec{\nabla}_{\vec{\xi}} u) \quad \text{for all } \vec{n} \in \mathbb{R}^d, \tag{2.19}$$

we can write

$$\vec{f}(u, \nabla_{\vec{x}} u) \cdot \vec{n} = \mu u_{\xi_1} =: f_{\vec{n}} \tag{2.20}$$

Hence, the multi-dimensional problem can be reduced to a one-dimensional problem into the direction normal to the element surface:

$$\vec{g}(\mu^{\pm}, u^{\pm}, \vec{\nabla}_{\vec{x}} u^{\pm}) \cdot \vec{n} =: g_{\vec{n}}(\mu^{\pm}, u^{\pm}, u_{\xi_1}^{\pm}), \tag{2.21}$$

where "−" and "+" denote the values at the grid cell interfaces from inside and outside of the considered grid cell.

In [10] we constructed a diffusion flux in one space dimension which is based on the solution of the generalized Riemann problem for linear diffusion equations and called it the dGRP flux (diffusive Generalized Riemann Problem). We also showed how to extend this numerical flux to nonlinear diffusion problems. In the following we extend this approach to discontinuous diffusion coefficients where the discontinuity is aligned with the grid. We consider first the linear diffusive generalized Riemann problem in this case and present the numerical fluxes $g_{\vec{n}}$ and $g_{\vec{n}}^a$ based on this local solution. These considerations also lead to some new insight extending the dGRP flux to nonlinear equations. In this case we may have a similar situation, since at grid cell interfaces the numerical solution may be discontinuous, that is, $u^+ \neq u^-, u_{\xi_1}^+ \neq u_{\xi_1}^-$, and the heat conduction coefficients may have the different limits $\mu^+ \neq \mu^-$ from both sides of the interface.

The computation of the numerical fluxes $g_{\vec{n}}$ and $g_{\vec{n}}^a$ is based on the initial value problem for the linear diffusion equation with piecewise linear data and piecewise constant diffusion coefficients

$$\begin{aligned}
&\frac{\partial}{\partial t} v = \lambda(\xi_1) \frac{\partial^2}{\partial \xi_1^2} v, \\
&v(\xi_1, 0) = \begin{cases} u^+ + \xi_1 u^+_{\xi_1}, & \text{for } \xi_1 > 0, \\ u^- + \xi_1 u^-_{\xi_1}, & \text{for } \xi_1 < 0, \end{cases} \\
&\lambda(\xi_1) = \begin{cases} \mu^+, & \text{for } \xi_1 > 0, \\ \mu^-, & \text{for } \xi_1 < 0. \end{cases}
\end{aligned} \tag{2.22}$$

As previously defined, ξ_1 denotes the coordinate into the normal direction of the grid cell surface. The exact solution of this initial value problem (2.22) is used to get information about the local behavior of the solution at the interface and to define the diffusion fluxes $g_{\vec{n}}$ and $g^a_{\vec{n}}$ as

$$g_{\vec{n}} = \frac{2[\![u]\!]\sqrt{\mu^+\mu^-}}{\sqrt{\Delta t}\sqrt{\pi}\left(\sqrt{\mu^+} + \sqrt{\mu^-}\right)} + \frac{\sqrt{\mu^+} f^-_{\vec{n}} + \sqrt{\mu^-} f^+_{\vec{n}}}{\sqrt{\mu^+} + \sqrt{\mu^-}}, \tag{2.23}$$

and

$$g^a_{\vec{n}} = (u_{S_k} - u^-)\mu^- \phi^-_{\xi_1} \tag{2.24}$$

with

$$u_{S_k} = \frac{\sqrt{\mu^+} u^+ + \sqrt{\mu^-} u^-}{\sqrt{\mu^+} + \sqrt{\mu^-}}. \tag{2.25}$$

The derivation of these fluxes can be found in Appendix A.

2.5. Space–time expansion

A question which is still open is how to get the values $u_i(\vec{x}, t)$ at the quadrature points in the space–time interval Q^n_i, which are needed as arguments for the flux functions in the evolution equation for the DOF (2.16). The numerical solution is only known at $t = t^n$. In the interval Q^n_i, we use instead a high order approximation $\tilde{u}_i(\vec{x}, t)$ of this solution obtained by considering a local Cauchy problem with initial condition $\tilde{u}_i(\vec{x}, t^n) = u_i(\vec{x}, t^n)$. This local Cauchy problem can be solved approximately as follows. We start with a Taylor expansion in space and time

$$\tilde{u}(\vec{x}, t) = u_i(\vec{x}_{\text{bary}}, t^n) + \sum_{j=1}^{N} \frac{1}{j!} \left((t - t^n) \frac{\partial}{\partial t} + (\vec{x} - \vec{x}_{\text{bary}}) \cdot \vec{\nabla} \right)^j u_i(\vec{x}_{\text{bary}}, t^n) \tag{2.26}$$

about the barycenter $\vec{x}_{\text{bary}}$ of the grid cell Q_i at the old time level t^n. This space–time Taylor expansion provides approximate values for $\tilde{u}$ and $\vec{\nabla}\tilde{u}$ at all space–time points $(\vec{x}, t) \in Q^n_i$, if all the values of the space–time derivatives at $(\vec{x}_i, t^n)$ are known.

While the pure space derivatives at $(\vec{x}_i, t^n)$ are readily available within the DG framework, the time derivatives and mixed space–time derivatives have to be computed using the so-called Cauchy–Kovalevskaya (CK) procedure. This procedure applies the evolution equation several times to re-write the time derivatives as space derivatives and is discussed in detail in the next subsection. The use of a Taylor expansion in space–time at the barycenter has already been proposed by Harten et al. [12] within the ENO finite volume framework. We note that the space–time expansion (2.26) has not necessarily to be performed in the conservative variable u, but in any other variable connected to u via a unique mapping. It may be easier and more efficient to build the space–time expansion in the temperature variable θ based on (2.1). As long as the variational formulation is based on the conservative form, the scheme is still exactly conservative.

2.6. Cauchy–Kovalevskaya procedure

If the space–time expansion about a grid cell barycenter $\vec{x}_{B_i}$ is based on the conservative form (2.5), we obtain for three space dimensions $d = 3$

$$\frac{\partial^{m+p+q+o}u}{\partial x_1^m x_2^p x_3^q t^o} = \frac{\partial^{m+p+q+o}(\mu(\vec{x}_{B_i},u)u_{x_1})}{\partial x_1^{m+1} x_2^p x_3^q t^{o-1}} + \frac{\partial^{m+p+q+o}(\mu(\vec{x}_{B_i},u)u_{x_2})}{\partial x_1^m x_2^{p+1} x_3^q t^{o-1}} + \frac{\partial^{m+p+q+o}(\mu(\vec{x}_{B_i},u)u_{x_3})}{\partial x_1^m x_2^p x_3^{q+1} t^{o-1}} \tag{2.27}$$

This equation is obtained for any set of natural numbers m, p, q, o by differentiating the governing Eq. (2.5) several times in space and time. On the left hand side the time derivative of order o appears, while all expressions on the right hand side contain time derivatives of the lower order $o-1$ only. Hence, with this relation all space–time derivatives of u can be computed in a successive way starting from pure space derivatives.

The structure of this algorithm is in a Fortran-like coding as

```
DO o = 1, (N-1)/2
  DO m = 0, N-o
    DO p = 0, N-o-m
      DO q = 0, N-o-m-p
        !Compute u_(o*t,m*xl ,p*x2 ,q*x3) from already computed
        !space-time derivatives
      ENDDO
    ENDDO
  ENDDO
ENDDO
```

In the exterior loop, we begin from $o = 1$ up to $\#\frac{N-1}{2}$, where N is the maximal degree of the polynomial basis functions, while in the inner loops the higher order space derivatives are calculated. Next we consider the CK-procedure for some special Eq. (2.1).

2.6.1. The linear case

If the material properties are constant in each element Q_i, that is, $c(\vec{x},\theta) = c_i$ and $k(\vec{x},\theta) = k_i$, and $\mu(\vec{x},\theta) = \mu_i = \frac{k_i}{c_i}$, the space–time expansion and the CK-procedure are directly done in u. In the CK loop, Eq. (2.27) can be easily evaluated, since $\mu =$ constant in each grid cell Q_i.

2.6.2. The nonlinear case

If μ is a function of u, the evaluation of Eq. (2.27) becomes more difficult. In the following, we describe how this can be done for two examples of material laws. We restrict ourselves for simplicity to one spatial dimension and name its coordinate x. The main tool for the CK-procedure is the generalized Leibniz rule in the form

$$\frac{\partial^{m+o}}{\partial x^m t^o}(fg) = \sum_{i=0}^{m}\sum_{l=0}^{o}\binom{m}{i}\binom{o}{l}\frac{\partial^{m-i+o-l}}{\partial x^{m-i}t^{o-l}}f\frac{\partial^{i+l}}{\partial x^i t^l}g \tag{2.28}$$

and its reformulation

$$\frac{\partial^{m+o}}{\partial x^m t^o}\left(\frac{f}{g}\right) = \frac{\partial^{m+o}}{\partial x^m t^o}(f) - \frac{1}{g}\underbrace{\sum_{i=0}^{m}\sum_{l=0}^{o}}_{i+l\neq m+o}\binom{m}{i}\binom{o}{l}\frac{\partial^{m-i+o-l}}{\partial x^{m-i}t^{o-l}}g\frac{\partial^{i+l}}{\partial x^i t^l}\left(\frac{f}{g}\right) \tag{2.29}$$

as a rule for differentiating quotients [9]. The functions $f = f(x,t)$ and $g = g(x,t)$ are always assumed to be sufficiently smooth.

2.6.3. Nonlinear examples

We first consider the one-dimensional equation

$$\frac{1}{\theta}\theta_t - \theta_{xx} = 0, \tag{2.30}$$

which may by written in conservative form

$$u_t - (\exp(u)u_x)_x = 0 \tag{2.31}$$

with the internal energy given by $u = \ln\theta$.

While the variational formulation is based on the conservative formulation (2.31), it is obvious that the CK-procedure based on this form is much more complicated than if it is based on the temperature Eq. (2.30). With Eq. (2.30) we get

$$\frac{\partial^{m+o}\theta}{\partial x^m t^o} = \frac{\partial^{m+o-1}\left(\theta\frac{\partial^2}{\partial x^2}\theta\right)}{\partial x^m t^{o-1}}, \tag{2.32}$$

which can easily be evaluated in the CK-procedure using the Leibniz rule (2.28). The space derivatives of θ can be approximated by L^2-projection of the function $\theta(u) = \exp(u)$ onto the functional basis with the desired order of accuracy.

Another example for the nonlinear case is

$$(1+\alpha\theta)\theta_t - \frac{\partial}{\partial x}((1+\beta\theta)\theta_x) = 0. \tag{2.33}$$

Here, the conservative variable u is given by $u = \theta + \frac{\alpha}{2}\theta^2$. As $\theta > 0$, the re-mapping $\theta(u)$ is uniquely defined by

$$\theta = \frac{-1+\sqrt{1+2\alpha u}}{\alpha}. \tag{2.34}$$

Eq. (2.33) becomes in the conservative variable u

$$u_t - \frac{\partial}{\partial x_1}\left(\frac{1+\beta\frac{-1+\sqrt{1+2\alpha u}}{\alpha}}{1+\alpha\frac{-1+\sqrt{1+2\alpha u}}{\alpha}}u_{x_1}\right) = 0. \tag{2.35}$$

Again, a CK-procedure in u would be very cumbersome. With Eq. (2.33), we can write

$$\frac{\partial^{m+o}\theta}{\partial x_1^m t^o} = \frac{\partial^{m+o-1}}{\partial x_1^m t^{o-1}}\frac{\frac{\partial}{\partial x_1}((1+\beta\theta)\theta_{x_1})}{1+\alpha\theta} \tag{2.36}$$

which is much easier to evaluate in the CK loop. We introduce an auxiliary variable $h1(x,t) = (1+\beta\theta)\theta_{x_1}$, whose space–time derivatives are computed and stored in the CK loop using Eq. (2.28). With $h1$ and its space–time derivatives, we can finally compute the space–time derivatives of θ by applying Eq. (2.29) within the same CK loop.

2.7. Local time-stepping

As the method proposed is an explicit scheme, it has to satisfy a time step restriction (3.42) for stability which depends on the local element size, the local order of accuracy and the local value of the approximation in the nonlinear case. Hence, the maximal time step given by this restriction may strongly vary in the computational domain. Standard explicit schemes have to use the minimal value over the whole domain as global time step to ensure stability. To overcome this inefficiency, the authors showed in [15] how to make use of the space–time approach and the locality of the discontinuous Galerkin discretization to introduce a *natural* arbitrary high order accurate local time-stepping. In the following, the algorithm is briefly described and adopted for the diffusion equations.

We give up the assumption that all grid cells run with the same time step and therefore we do not have any longer a common time level. Let us denote the actual local time level in grid cell Q_i by t_i^n. The degrees of freedom $\hat{u}_i^n$ represent the solution at t_i^n in this grid cell. Furthermore, each cell may evolve in time with its local time step Δt_i^n which has to satisfy the local stability restriction. The stability restriction is discussed in the next subsection. With Δt_i^n, the next local time level in Q_i is given as

$$t_i^{n+1} = t_i^n + \Delta t_i^n. \tag{2.37}$$

In order to evolve the $\hat{u}_i$ from time level t_i^n to t_i^{n+1}, the right hand side of the variational formulation Eq. (2.16) has to be determined for every Q_i. To guarantee that this is done in a proper way, the succession of evolving elements has to be controlled.

To illustrate how the time-stepping procedure works, we sketched in one space dimension a sequence of four time steps with three adjacent grid cells in Fig. 1 starting from a common time level $t_1^0 = t_2^0 = t_3^0 = t^0 = 0$. After the determination of all local time steps, which are assumed to be different in our example, the space–time Taylor expansions are calculated in each element. This results in an approximate solution $\tilde{u}$ in every space–time cell Q_i^n - in our example we have $i = 1, 2, 3$. These space–time polynomials are stored. Thus the variables that hold the degrees of freedom (DOF) $\hat{u}_i^0$ at the old time level t_i^0 may be overwritten in subsequent steps in order to evolve them to DOF at the new time level $\hat{u}_i^1$. For clarity we call DOF without physical meaning, obtained by partial evaluation of the integrals in (2.16), by $\hat{u}_i^*$. In a first step the flux volume integral in (2.16) is evaluated for each element Q_i and its contribution is simply added to $\hat{u}_i^*$. In our example this state is given in the upper left corner of Fig. 1. For each space–time grid cell, the space–time polynomial is determined and the contribution of the volume integral is already contained in the $\hat{u}_i^*$. The surface flux contributions involving neighboring grid cells are considered in the next step.

The local time-stepping algorithm relies on the following evolve condition. The update of the DOF in Q_i can be finished, if

$$t_i^{n+1} \leqslant \min\{t_j^{n+1}\}, \quad \forall j : Q_j \cap Q_i \neq \emptyset \tag{2.38}$$

is satisfied, because all the neighboring data for the flux calculation are available. In our example, the only grid cell satisfying this condition is Q_2. So Q_2 can be evolved to the next time level t_2^1. To do so, the flux contributions at the right and left cell interface are computed and simply added to the DOF $\hat{u}_2^*$. The flux integrals are calculated using Gauss quadrature formulae from $t = t_2^0$ to $t = t_2^1$ at the right interface $\partial Q_{2+\frac{1}{2}}$ and the left interface $\partial Q_{2-\frac{1}{2}}$. The arguments for the numerical flux functions at time Gaussian points are obtained from the left and right space–time polynomials. If both flux contributions are added to $\hat{u}_2^*$, the update is completed and the DOF of Q_2 at the new time level t_2^1 are known, $\hat{u}_2^*$ become $\hat{u}_2^1$.

In order to avoid the calculation of interface fluxes twice and to get an efficient conservative scheme, the flux contributions computed to evolve the element 2 are simultaneously added with the minus sign also to the DOF of the neighboring elements resulting in updated values $\hat{u}_1^*$ and $\hat{u}_3^*$. For Q_2 we proceed as in the first time step. A new space–time polynomial is constructed on $Q_2 \times [t_2^1, t_2^2]$ and the volume integral contribution is added to the local DOF $\hat{u}_2^1$, now named by $\hat{u}_2^*$. We are then in the situation sketched in the upper right corner of Fig. 1. For given boundary values, now Q_1 satisfies the evolve condition and can be advanced to t_1^1. As

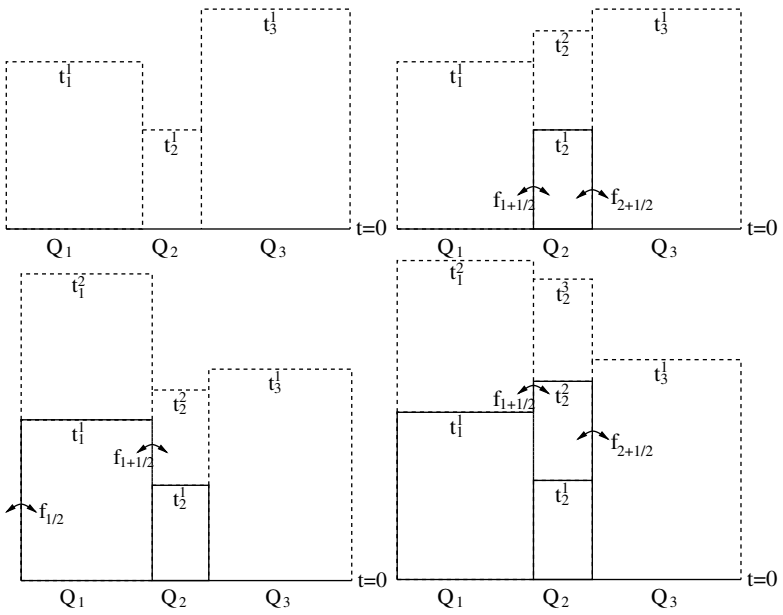

Fig. 1. Sequence of steps 1–4 of a computation with three different elements and local time-stepping.

before, the volume integral contribution was already computed and added in a first step. But in this case, also a part of the flux contributions has already been added to the $\hat{u}_1^*$ during the previous evolution of Q_2. Thus, only the missing flux contributions, which are sketched in the lower left corner of Fig. 1, have to be added. Namely, on the interface $\partial Q_{1+\frac{1}{2}}$, the flux integral has to be computed with a quadrature formula from t_2^1 to t_1^1. After the step of calculating the missing pieces of the flux surface integrals on both sides the update of Q_1 is completed and $\hat{u}_1^*$ get $\hat{u}_1^1$. As before, the flux integral computed on this shared interface is not only added to $\hat{u}_1^*$, but also to the $\hat{u}_2^*$. For our example we are now at the left lower diagram.

In general, the time interval, for which the flux contribution at the interface shared by an element Q_i and an adjacent element Q_j has to be computed in the evolution step from $\hat{u}_i^*$ to $\hat{u}_i^{n+1}$, is

$$[t_{ij}^{\bigstar}, t_i^{n+1}] = [\max(t_i^n, t_j^n), t_i^{n+1}] \tag{2.39}$$

After the evolution step the whole update is completed for Q_i. Beside the new time levels and the space–time polynomial from the neighboring grid cells no additional information is necessary for the whole evolution step. In this manner, the algorithm continues by searching for elements satisfying the evolve condition (2.38). All elements are evolved in a suitable order by evaluating the different terms of the discrete variational formulation (2.16) in an optimal order. At each time, the interface fluxes are defined uniquely for both adjacent elements, making the scheme exactly conservative. In our example we can next advance and complete the update of grid cell Q_2 again and proceed the calculation, see Fig. 1.

The presented local time-stepping algorithm minimizes the total number of time steps for a computation with fixed end time. However in some cases where the difference of time levels of adjacent grid cells are very small compared to the local time steps, the efficiency of the presented local time-stepping algorithm may decrease. To overcome this deficiency we locally synchronize the time levels of those identified cells. It is also no problem to introduce some common global time levels as needed for example at the end time of the computation.

3. Matrix stability analysis for the linear 1D case

As every explicit time-stepping scheme, the STE-DG scheme has a time step restriction for stability. In this subsection, we determine the maximal stability region of the scheme applied to the one-dimensional linear heat conduction equation

$$u_t + \mu u_{xx} = 0 \quad \text{with } \mu \in \mathbb{R}^+. \tag{3.40}$$

The stability analysis of the STE-DG scheme is performed for global time-stepping as well as for local time-stepping.

To analyze the stability of the scheme, a periodic problem with a given spatial discretization is considered. As the problem (3.40) is linear, one can construct a matrix $\boldsymbol{W}$ such that

$$\hat{u}^{\text{new}} = \boldsymbol{W}\hat{u}^{\text{old}}, \tag{3.41}$$

where $\hat{u}^{\text{old}}$ denote DOF at a common time level t^{old} and $\hat{u}^{\text{new}}$ denote DOF at a common time level t^{new} with $t^{\text{new}} > t^{\text{old}}$. $\boldsymbol{W} = \boldsymbol{W}(\Delta t_i)$ depends on the time steps Δt_i of each element Q_i. Following the matrix method of stability analysis described in [14], the scheme is stable, if the spectral radius $\rho(\boldsymbol{W})$ is lower or equal to 1.

We first consider uniform grid spacing and uniform polynomial order, thus, $\Delta x = \text{const}$ and $\Delta t = \text{const}$ in the whole computational domain. For an explicit DG scheme discretizing equation (3.40), a stability restriction for the time step has the form

$$\Delta t \leqslant \beta(N)\frac{\Delta x^2}{(2N+1)^2\mu\sqrt{d}}, \tag{3.42}$$

where N again denotes the polynomial degree and the coefficient β is a function of N. To transfer the formula to the multi-dimensional case we also included the dimension, here we have $d = 1$. For $d > 1$, we define Δx of an element Q_i by two times the smallest distance of its barycenter to one of its surfaces. With Eq. (3.42), we can re-write the numerical flux (2.23) for the case of constant μ in the form

$$g_{\vec{n}} = \frac{2(2N+1)\mu d^{0.25}}{\Delta x\sqrt{\beta}\sqrt{\pi}}[\![u]\!] + \{f_{\vec{n}}\} =: \eta[\![u]\!] + \{f_{\vec{n}}\}. \tag{3.43}$$

Using this numerical flux, we obtain stability numbers β as presented in Table 1.

3.1. Optimization of the time step and the penalization parameter

In the following we introduce a penalization parameter into the diffusion flux (3.43). This can be done in a simple way, if we distinguish between the β occurring in the time step restriction (3.42) from the one occurring in the numerical flux (3.43), which we call now penalization parameter $\tilde{\beta}$. In the following we compute for every polynomial degree N the stability number β for varying $\tilde{\beta}$. The resulting stability regions are presented in Fig. 2 for polynomial degrees $N = 1$ to $N = 7$.

We can see, that the maximal β can even be slightly improved compared to the dGRP flux in Table 1 by choosing an optimal $\tilde{\beta}$. The stability regions are similar for each N. For large values of $\tilde{\beta}$ the jump penalization constant η becomes too small and the schemes are unconditionally unstable. For small values of $\tilde{\beta}$, the β decreases linearly with $\tilde{\beta}$, and thus allowing only small time steps. This corresponds well to the stiffness introduced by a large penalization constant in the equation when solving stationary heat equation with the SIP-DG method. In between, there is an interval for $\tilde{\beta}$, in which β is constant and has its maximum, we denote this value by $\beta_{\max}$. We further denote the upper limit of the $\tilde{\beta}$ interval by $\tilde{\beta}_{\max}$ and the lower limit by $\tilde{\beta}_{\min}$. Hence, in order to get the maximal time step, we should choose a $\tilde{\beta}$ such that $\tilde{\beta}_{\min} \leqslant \tilde{\beta} \leqslant \tilde{\beta}_{\max}$. The values of $\tilde{\beta}_{\min}$ and $\tilde{\beta}_{\max}$ as well as the value of $\beta_{\max}$ corresponding to Fig. 2 are listed in Table 2.

Table 1
Stability numbers of the STE-DG scheme

N	1	2	3	4	5	6	7
β	1.46	0.8	0.40	0.24	0.16	0.12	0.09

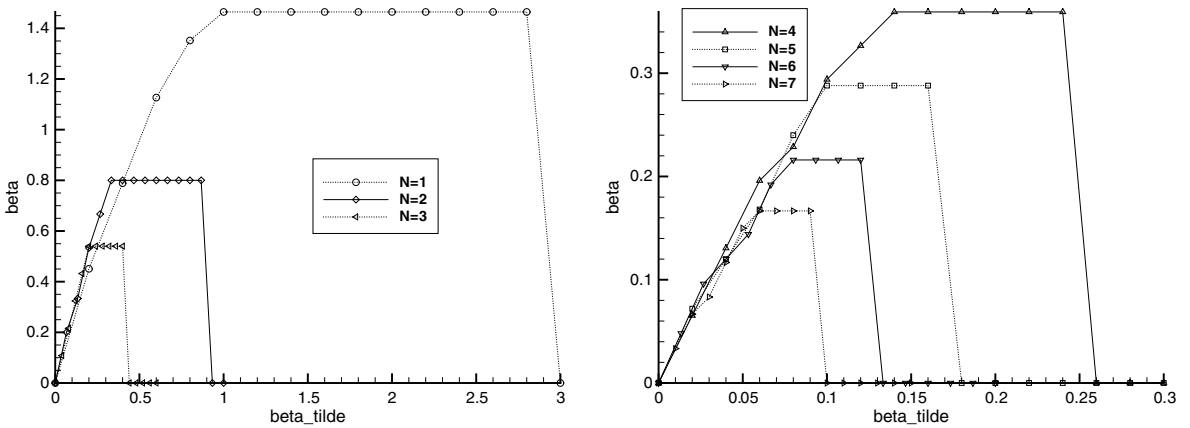

Fig. 2. Stability regions β over $\tilde{\beta}$ for $N = 1$ to $N = 7$ on a uniform grid.

Table 2
Stability numbers of the optimized STE-DG scheme

N	1	2	3	4	5	6	7
$\beta_{\max}$	1.46	0.8	0.54	0.355	0.28	0.21	0.16
$\tilde{\beta}_{\min}$	1.0	0.33	0.20	0.14	0.10	0.08	0.06
$\tilde{\beta}_{\max}$	2.8	0.86	0.40	0.24	0.16	0.12	0.09

3.2. Stability and choice of the penalty constant for a non-uniform grid

If the grid cell size Δx, the polynomial degree N or the heat conduction coefficient μ jump at the interface S_k, the jump penalization factor η jumps as well when the optimal $\tilde{\beta}^{\pm} = \tilde{\beta}^{\pm}_{\max}(N^{\pm})$ is chosen. In this case, we get from Eq. (2.23) and using Eq. (3.42) the values:

$$\eta^{\pm} = \frac{2\sqrt{\mu^{+}\mu^{-}}}{\sqrt{\Delta t^{\pm}}\sqrt{\pi}\left(\sqrt{\mu^{+}}+\sqrt{\mu^{-}}\right)} = \frac{2(2N^{\pm}+1)\sqrt{\mu^{+}\mu^{-}}\sqrt{\mu^{\pm}}d^{0.25}}{\Delta x^{\pm}\sqrt{\tilde{\beta}^{\pm}}\sqrt{\pi}\left(\sqrt{\mu^{+}}+\sqrt{\mu^{-}}\right)} \tag{3.44}$$

To retain exact conservation, a unique η_{S_k} has to be defined at the interface S_k. For a fixed given η_{S_k}, the effective values of $\tilde{\beta}^{\pm}$ are given for the adjacent elements by

$$\tilde{\beta}^{\pm} = \frac{4(2N^{\pm}+1)^2\mu^{+}\mu^{-}\mu^{\pm}\sqrt{d}}{\Delta x^{\pm 2}\eta^2_{S_k}\pi\left(\sqrt{\mu^{+}}+\sqrt{\mu^{-}}\right)^2}. \tag{3.45}$$

We now postulate that the point $(\tilde{\beta},\beta)$ has to lie within the stability regions in Table 2 *locally* for both grid cells. The validity of this requirement in the sense that it gives save estimations of time steps and penalty parameters is confirmed by discrete stability analysis using the matrix method for a large number of non-conforming grid configurations. Otherwise the approximate solution becomes unstable. This requirement leads to the two conditions

$$\tilde{\beta}^{\pm} \leqslant \tilde{\beta}^{\pm}_{\max}. \tag{3.46}$$

From this the following condition on η_{S_k} is obtained:

$$\eta_{S_k} \geqslant \frac{2\sqrt{\mu^{+}\mu^{-}}d^{0.25}}{\sqrt{\pi}\left(\sqrt{\mu^{+}}+\sqrt{\mu^{-}}\right)} \max\left(\frac{(2N^{\pm}+1)\sqrt{\mu^{\pm}}}{\sqrt{\tilde{\beta}^{\pm}_{\max}}\Delta x^{\pm}}\right). \tag{3.47}$$

Hence, the minimal value of η_{S_k} that satisfies this inequality should be chosen in order to maximize the time step. The maximal time step Δt_i of a grid cell Q_i is then computed using the diagrams in Fig. 2. To do this, the minimal effective $\tilde{\beta}$ on ∂Q_i is determined first:

$$\tilde{\beta}_{i,\mathrm{eff}} = \min_{\partial Q_i}\frac{4(2N_i+1)^2\mu^{+}\mu^{-}\mu^{-}\sqrt{d}}{\Delta x_i^2\eta^2_{S_k}\pi\left(\sqrt{\mu^{+}}+\sqrt{\mu^{-}}\right)^2} = \frac{(2N_i+1)^2}{\Delta x_i^2}\min_{\partial Q_i}\left(\mu^{-}\min\left(\frac{\tilde{\beta}^{\pm}_{\max}\Delta x^{\pm 2}}{(2N^{\pm}+1)^2\mu^{\pm}}\right)\right), \tag{3.48}$$

with the minimal η_{S_k}. Then, the maximal stable β^i can be determined via the stability diagrams. For our practical simulations we simplified the $(\tilde{\beta},\beta)$-diagrams by assuming a straight line in the interval $[0,\tilde{\beta}_{\min}]$ and $\tilde{\beta}_{\max}$ from 0 to $\beta_{\max}$ and obtained the simple formula

$$\beta_i = \beta_{\max}(N_i)\min\left(1,\frac{\tilde{\beta}_{i,\mathrm{eff}}}{\tilde{\beta}_{\min}(N_i)}\right). \tag{3.49}$$

for the computation of β.

With the minimal η_{S_k} from (3.47) and the time steps computed via (3.49) we performed the matrix stability analysis in the case $N = 3$ for some non-uniform grids and local time-stepping. The spectral radius of $\boldsymbol{W}$ was computed for varying $\beta_{\max}$ with $\tilde{\beta}_{\min}$ and $\tilde{\beta}_{\max}$ as given in Table 2. The results as presented in Fig. 3 indicate that the most restrictive $\beta_{\max}$ is obtained for the case of uniform grid. This observation held in all our calculations, for other considered space grids and other orders of accuracy as well. Also in numerical experiments in two and three space dimensions, we never encountered problems even with jumping μ or local varying N. Hence, we state that using the numerical fluxes and time step restrictions as derived in this section are reliable for computations on non-uniform grids with local time-stepping.

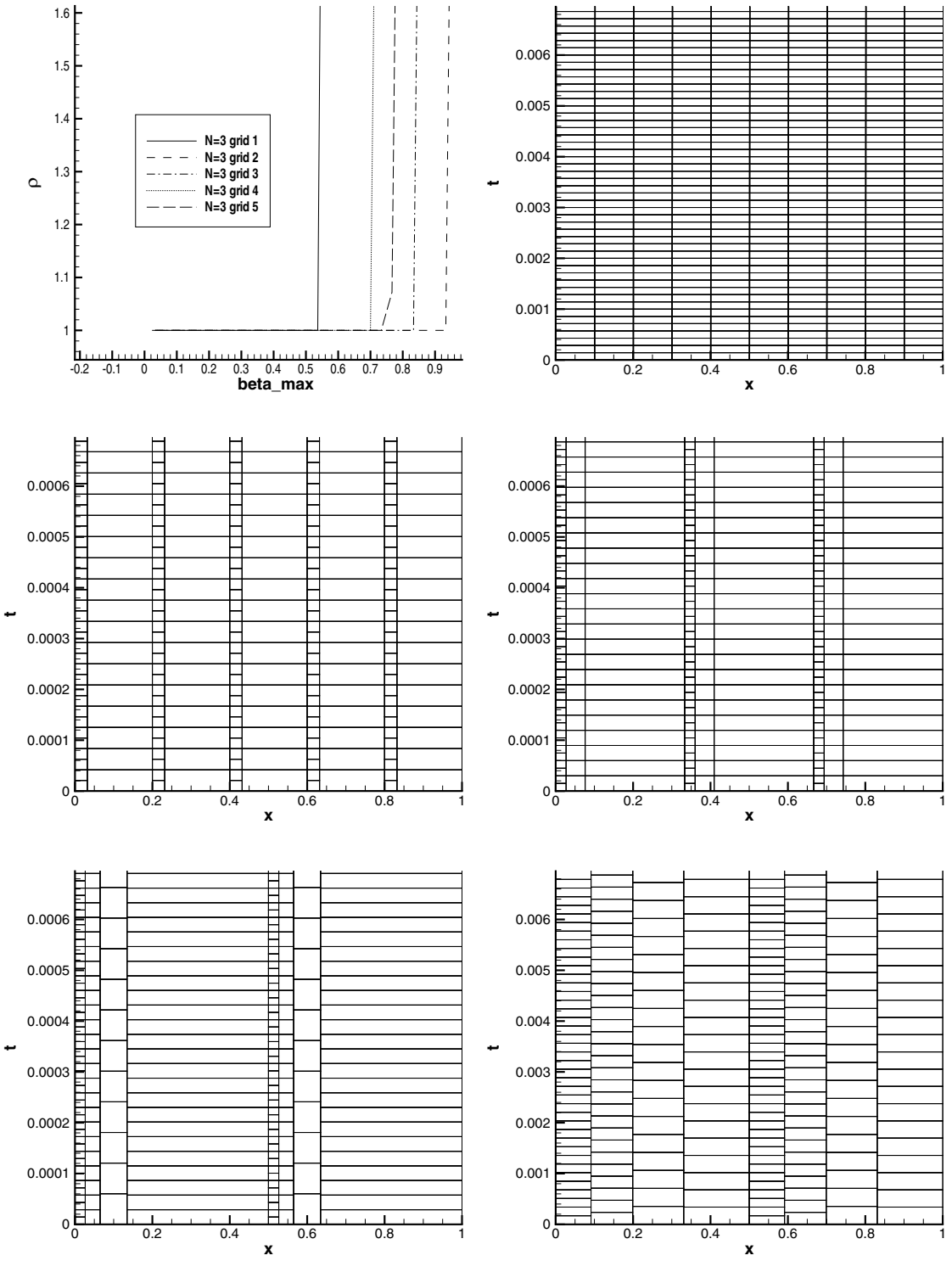

Fig. 3. $\rho(\boldsymbol{W})$ as function of $\beta_{\max}$ for space–time grids 1–5, space–time grids 1–5.

4. Numerical results

4.1. One-dimensional heat conduction with a robin boundary condition

The first test case is a linear heat conduction problem in one space dimension and models the transient heat distribution in a wall which separates two states with different constant temperatures. The problem is assumed to be one-dimensional with constant $\mu = 0.5$ on the space domain $\Omega = [0, 1]$. This test case with given analytical solution validates the numerical method completed by Robin boundary conditions. On both domain boundaries Ω_{C1} at $x = 0$ and Ω_{C2} at $x = 1$, we impose Robin boundary conditions of the form

$$\alpha_{Ci}(u_{Ci} - u(x)) + \mu \frac{\partial}{\partial x}(u) = 0 \tag{4.50}$$

with $\alpha_{C1} = 5.0, \alpha_{C2} = 6.0, u_{C1} = 0$ and $u_{C2} = 0.5$. The initial condition is $u = 1$ on Ω. An analytical solution is given in [6]. We compare numerical results for this problem computed on different space discretizations with 2, 4, 8, and 16 grid cells for the polynomial degree $N = 4$ and $N = 5$. The comparison with the exact solution shows the decrease of the error and gives information about the experimental order of convergence. Here, we used a coarse grid in combination with high order schemes. The L_2-error between the numerical solution and the exact one at the time $t = 1$ is given in Table 3. The results clearly indicate that the optimal order of convergence is achieved.

4.2. Two-dimensional convergence study

The second test case is a convergence study in two space dimensions for the linear heat conduction Eq. (2.5). The computational domain is $\Omega = [0, 1] \times [0, 1]$. The initial condition is $u = 0$ on Ω. At the domain boundaries $x_1 = 1$ and $x_2 = 1$, we impose the Dirichlet conditions $u = 1$, while at $x_1 = 0$ and $x_2 = 0$, we impose homogeneous von Neumann conditions $\frac{\partial}{\partial \vec{n}} u = 0$. The analytical transient solution is given in [18]. Results of a convergence study in the two-dimensional case at $t = 1$ are given in Table 4. They clearly show that the

Table 3
Experimental order of convergence for test case 4.1 for the polynomial degree $N = 4$ and $N = 5$

$N = 4, n_{\text{Cells}}$	2	4	8	16
$\|u - u_{\text{exact}}\|_{L_2}$	1.32E−05	3.83E−07	1.09E−08	3.21E−10
$\mathcal{O}_{L_2}$		5.10	5.13	5.09
$N = 5, n_{\text{Cells}}$	1	2	4	8
$\|u - u_{\text{exact}}\|_{L_2}$	6.61E−05	1.05E−06	1.59E−08	2.53E−10
$\mathcal{O}_{L_2}$		5.97	6.05	5.98

Table 4
Error and experimental order of convergence for test case Section 4.2 and $N = 2$, $N = 6$, and $N = 7$

$N = 2, n_{\text{Cells}}$	4	16	64	256
CPU-time (s)	1.2	7.7	49	292
$\|u - u_{\text{exact}}\|_{L_2}$	1.26E-03	1.36E-04	1.58E-5	1.93E-6
$\mathcal{O}_{L_2}$		3.21	3.10	3.03
$N = 6, n_{\text{Cells}}$	1	4	16	64
CPU-time (s)	0.37	6.0	93	1700
$\|u - u_{\text{exact}}\|_{L_2}$	4.67E−06	4.05E−08	3.29E−10	2.60E−12
$\mathcal{O}_{L_2}$		6.85	6.94	6.99
$N = 7, n_{\text{Cells}}$	1	4	16	64
CPU-time (s)	2.1	31.25	320	5200
$\|u - u_{\text{exact}}\|_{L_2}$	3.59E−07	1.49E−09	6.00E−12	1.43E−14
$\mathcal{O}_{L_2}$		7.92	7.96	7.95

designed order of accuracy is obtained. The numerical results were obtained by using quite coarse Cartesian grids. Here, we applied schemes with the polynomial degrees $N = 2, N = 6$ and $N = 7$. Comparing CPU-time and error norm of the computation $N = 2, n_{\text{Cells}} = 256$ to those of the computation $N = 7, n_{\text{Cells}} = 1$, we clearly see the gain of a high order method: the high order simulation gives better result in much lower computational time compared to the low order simulation.

4.3. Nonlinear example

We next consider two nonlinear examples in one space dimension for the validation. In the first case, the governing equation is given by Eq. (2.30) on the space domain $\Omega = [0, 1]$. The initial temperature distribution is given by

$$\theta(x, 0) = 1 - \frac{1}{2}x^2, \tag{4.51}$$

the boundary conditions at $x = 0$ and $x = 1$ are the von Neumann condition

$$\frac{\partial\theta}{\partial n}(x, t) = 0. \tag{4.52}$$

The analytical solution is given in [11] and reads as

$$\theta(x, t) = \frac{1}{1 + t}\left(1 - \frac{1}{2}x^2\right). \tag{4.53}$$

A convergence study at $t = 1$ for this problem is presented in Table 5. We show there the third and fourth order accurate STE-DG scheme on 2, 4, 8, and 16 grid cells. Also for this nonlinear problem, the optimal order of convergence can be observed as expected.

We also applied the scheme to the nonlinear problem (2.33) for validation. For the initial condition $\theta(x, 0) = 0$ and the boundary conditions $\theta(0, t) = 1$ and $\theta(1, t) = 0$ the numerical results coincide very well with those presented in [11] for various finite difference schemes.

4.4. Laser heat treatments

As a more advanced problem we applied the STE-DG scheme to simulate the heating of a square plate induced by laser treatment. This process can be modeled by a linear heat conduction equation. An analytical solution and detailed description of the problem can be found in [1]. For all calculations presented here, the computational domain was $\Omega = [-1, 1] \times [0, 2]$. The impinging of the laser beam is mathematically modeled by a heat flux distribution $f(x, y)$ on the upper side $(x; y = 2)$ of the plate and defines there the boundary condition for the simulation. The beam is either fixed at a certain position or may move parallel to the plate with constant velocity $(\vec{v} \neq 0)$. In the case of a stationary laser beam, the flux has a Gaussian distribution centered at $x = x_0$:

$$f(x, y = 2) = -\eta \frac{P}{\sqrt{2\pi w^2}} \exp\left(-\frac{1}{2}\frac{(x - x_0)^2}{w^2}\right) \tag{4.54}$$

where P denotes the nominal power of the beam and η is a coefficient that describes the laser absorption in the material, this is, the fraction of energy that is effectively absorbed and not reflected. Although strictly speaking

Table 5
Experimental order of convergence for the nonlinear test case 4.3 and $N = 2$ and $N = 3$

$N = 2, n_{\text{Cells}}$	2	4	8	16
$\|u - u_{\text{exact}}\|_{L_2}$	6.98E−04	1.06E−04	1.41E−05	1.80E−06
$\mathcal{O}_{L_2}$		2.72	2.91	2.97
$N = 3, n_{\text{Cells}}$	2	4	8	16
$\|u - u_{\text{exact}}\|_{L_2}$	1.06E−04	9.17E−06	6.49E−07	4.21E−08
$\mathcal{O}_{L_2}$		3.54	3.82	3.94

w is the standard deviation of the Gauss distribution, it will be referred to as the width of the beam. The minus sign in Eq. (4.54) accounts for the laser heat flux being an inward boundary flux.

If the beam moves with constant velocity v starting from $x = x_0$ along the upper side of the plate, f is given by

$$f(x,y,t) = -\eta \frac{P}{\sqrt{2\pi w^2}} \exp\left(-\frac{1}{2}\frac{((x-x_0)-vt)^2}{w^2}\right) \tag{4.55}$$

At all the other boundaries an adiabatic or zero-flux condition was imposed.

Numerical results are presented for both cases. We choose a nominal power $P = 1.5$ W and the absorption coefficient $\eta = 0.8$, the values for the material properties were: $K = 1\ W/(\mathrm{m}\,K)$, $\mu = 0.5\ \mathrm{m}^2/\mathrm{s}$. A uniform temperature $u(\vec{x}, 0) = 100$ K was imposed as initial condition.

All calculations were performed in the interval $0\ \mathrm{s} \leqslant t \leqslant 10$ s, and the polynomial degree was chosen to $N = 5$ on 16×16 grid cells in the computational domain Ω. Note that the chosen grid is quite coarse for this problem.

4.4.1. Stationary beam fixed at $x = 0$

The simulated Gaussian shaped beam has the width $w = 0.075$. The resulting temperature map obtained is shown together with the analytical solution in Figs. 4 and 5. The good agreement between the numerical

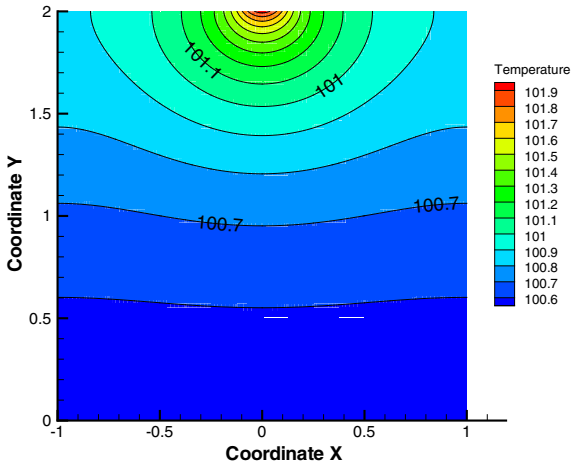

Fig. 4. Temperature contour in $t = 5$ s for the fixed beam with $w = 0.075$: numerical solution.

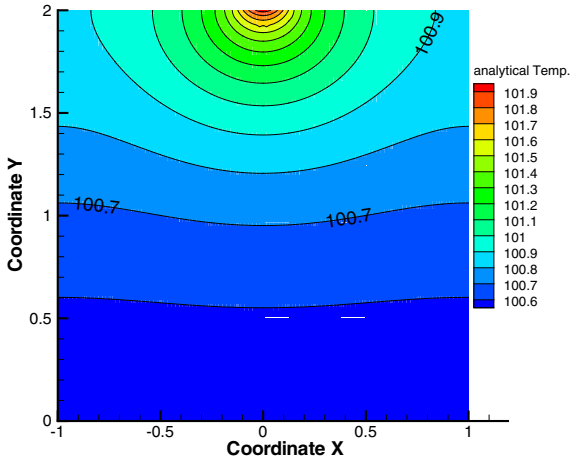

Fig. 5. Temperature contour in $t = 5$ s for the fixed beam with $w = 0.075$: analytical solution.

results and the analytical solution is quite obvious. In order to determine the influence of the width of the beam w we varied this parameter. Fig. 6 shows the temperature profile along the upper side of the plate for two values of the beam width. In both cases the results agree very well with the analytical solutions.

4.4.2. Beam moving with constant velocity ($\vec{v} \neq 0$)

Figs. 7 and 8 show now temperature maps for the beam moving along the upper side of the square with velocity $v = 0.04$ and beam width $w = 0.075$. The initial position was the center of the upper boundary of the square. Again, a good agreement with the analytical solution is observed. A variation of the width of the beam w is shown in Fig. 9.

4.5. Transient heat conduction in rewritable optical disks

During initialization and writing on a rewritable optical disk by a laser the disk may be heated up to 700 °C. Within the production process the amorphous sputtered phase change alloy layer has to be crystallized. The objective of such a numerical simulation is to get information about the temperature dependent reflectivity

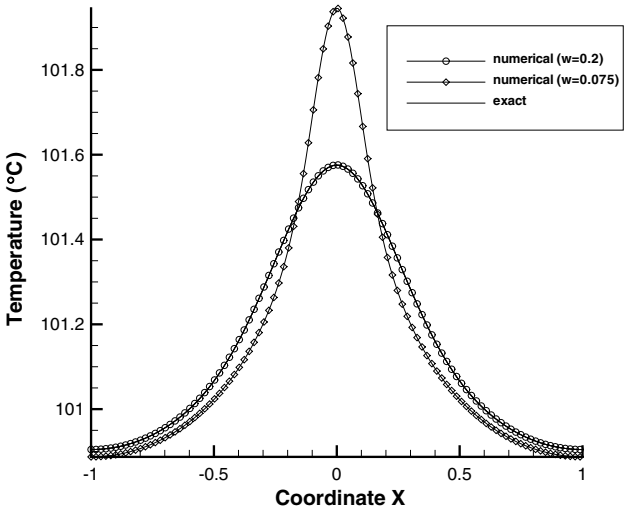

Fig. 6. Temperature profiles along the upper bound of the square for different beam widths w for a simulation with 16×16 elements.

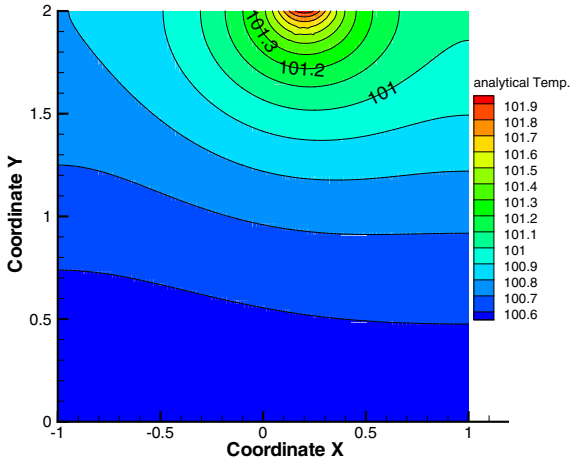

Fig. 8. Temperature contour in $t = 5$ s for the moving beam with $v = 0.04$ and $w = 0.075$: analytical solution.

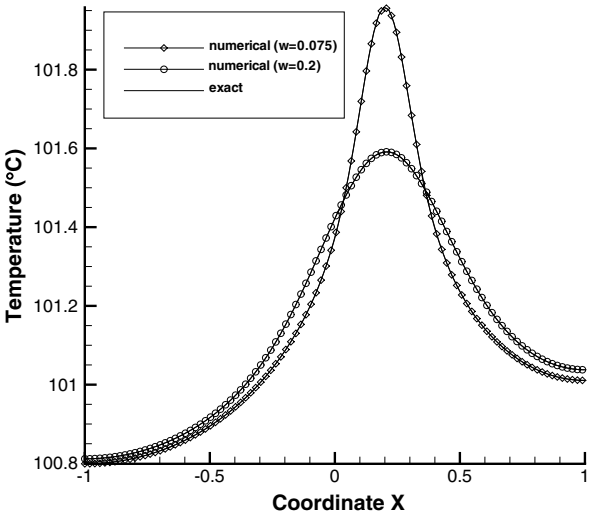

Fig. 9. Temperature profiles along the upper bound of the square for the moving beam for different beam widths w for a simulation with 16×16 elements.

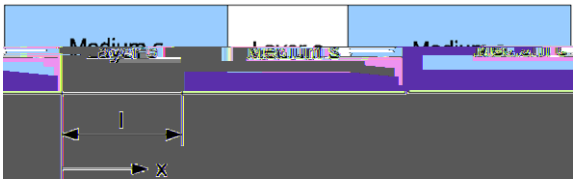

Fig. 10. Sketch of the one-dimensional geometry.

and the warpage of the disk during the process. A simple mathematical model for this process was proposed and analyzed by van der Tempel in [19]. Neglecting lateral heat conduction the problem may be reduced to one space dimension. The model is then given by two semi-infinite media separated by a layer which is heated by a laser beam. This situation is sketched in in Fig. 10. A layer o with thickness l is placed between two semi-infinite media c and s with uniform initial temperature T_0. As the heat generating layer has different material properties than the surrounding media, the differences in the heat conduction coefficients have to be taken into account. For this model it is furthermore assumed that

- each medium has constant uniform thermal properties: conductivity k, density ρ, and specific heat c_p,
- the thermal contact at all interfaces is perfect,
- conduction can be modeled by Fourier's law.

The energy equations for the heat generating layer between the two media reads then as

$$\frac{\partial T_c}{\partial t} = \alpha_c \frac{\partial^2 T_c}{\partial x^2} \tag{4.56}$$

$$\frac{\partial T_0}{\partial t} = \alpha_0 \frac{\partial^2 T_0}{\partial x^2} + vG(t - t_0) \tag{4.57}$$

$$\frac{\partial T_s}{\partial t} = \alpha_s \frac{\partial^2 T_s}{\partial x^2} \tag{4.58}$$

where t_0 is the time, when the center of a Gaussian radiative heating distribution passes, $v = \frac{q''}{l\rho c_p}$ is the heating rate. Hence, we have different temperature equations in the different materials and and a source term in the layer. The heating rate is given by a Gaussian distribution

$$G(t) = \sqrt{\frac{2}{\pi}} e^{-2\left(\frac{t}{\tau}\right)^2} \tag{4.59}$$

with effective heating time τ. As initial conditions the constant temperature T_0 is prescribed in the whole domain. Physical boundary conditions of the problem are given at infinity in the form

$$\lim_{x \to -\infty} T_c = \text{finite} \quad \lim_{x \to \infty} T_s = \text{finite}. \tag{4.60}$$

We assume a perfect thermal contact between the different media. Hence, the numerical simulations should show the continuity of the solution at the interfaces

$$T_c(0,t) = T_0(0,t) \quad T_0(l,t) = T_s(l,t) \tag{4.61}$$

as well as the continuity of the heat flux

$$k_c \frac{\partial T_c}{\partial x}(0,t) = k_0 \frac{\partial T_0}{\partial x}(0,t) \quad k_0 \frac{\partial T_0}{\partial x}(l,t) = k_s \frac{\partial T_s}{\partial x}(l,t) \tag{4.62}$$

Because these conditions are already included in the construction of the dGRP heat flux, these relations should be automatically reproduced.

The parameters in our calculations are chosen as follows: The thickness of the layer is $l = 0.27 \times 10^{-6}$ m, the initial temperature is $T_0 = 300$ K, the tangential heating rate distribution of the laser beam has a Gaussian

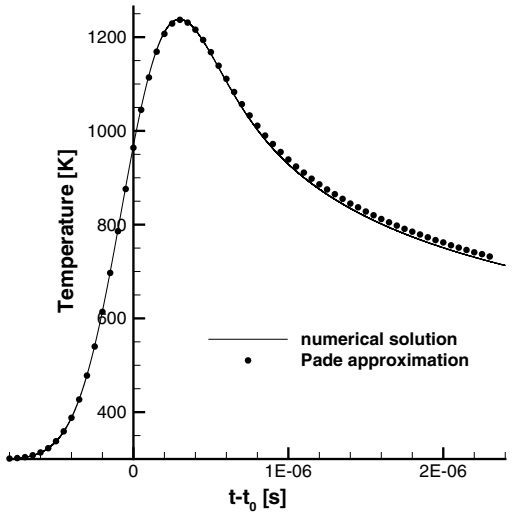

Fig. 11. Comparison of stack temperature calculation.

distribution with radiative heat flux $q'' = 3.9 \times 10^9\ \mathrm{W/m^2}$, effective heating time $\tau = 0.5\ \mu s$ and the time $t_0 = 0.8 \times 10^{-6}$ s at which the center of the Gaussian passes.

	Medium c	Layer o	Medium s
$H = \sqrt{k\rho c_p}$ ($\mathrm{W\sqrt{s}/m^2K}$)	750	3026	750
Diffusivity α ($\mathrm{m^2/s}$)	1.19×10^{-7}	1.59×10^{-6}	1.19×10^{-7}
Thickness l (m)		0.27×10^{-6}	

The computed data is compared to the results given in [19]. Here, the problem was solved by a Laplace-transformation with a series exact solution and a Pad like approximation. Fig. 11 shows the comparison of the results for the stack temperature.

5. Conclusions

In this paper we propose an explicit discontinuous Galerkin scheme, called the STE-DG scheme, for the discretization of diffusion equations in the space–time domain of arbitrary high order of accuracy in space and time. The scheme relies on a weak formulation of the diffusion equation introduced in [10] based on two partial integrations of the diffusion fluxes. Numerical fluxes at cell interfaces are defined using a local exact solution of an initial value problem with piecewise linear data. In this paper, we considered the case of discontinuous diffusion coefficients at grid cell boundaries, which either occurs at interfaces between materials or in the nonlinear case. A basic building block of the STE-DG scheme is the Cauchy–Kovalevskaya procedure. Although the DG scheme is always formulated in conservative variables, we show that in the Cauchy–Kovalevskaya procedure one may change to other variables which are related to the conservative variables by a unique mapping. This can be of advantage, as heat conduction equations have often a much simpler form in terms of the temperature.

For this explicit scheme, the size of the time step is limited by a stability condition. The stability was analyzed using the matrix method, and stability numbers for several scheme orders are given. Using this stability analysis, the jump penalization parameter was optimized. A special feature of the STE-DG scheme is the possibility of introducing a time-consistent, fully conservative local time-stepping without significant computational overhead. Following the stability analysis for the uniform case, the choice of the jump penalization parameter and the maximum stable time step are defined. Matrix stability analysis for non-uniform grid configurations confirm these choices. The local time-stepping strongly enhances the efficiency in all situations where the cell size or the element order vary over the computational domain and makes explicit schemes interesting for transient calculations.

In order to validate the scheme, numerical experiments are presented. The experimental order of convergence is tested for linear and nonlinear problems with different boundary conditions and with discontinuous material constants. As our first applications we presented simulations of the transient temperature distribution caused by laser coating of a flat plate and by the initialization of a compact disc.

Acknowledgments

This project was supported by the Deutsche Forschungsgemeinschaft (DFG) in the context of the Graduiertenkolleg GRK 1095/1. The authors would further like to thank Jens von Wolfersdorf for his support and discussions in defining good test cases and Markus Boger for their numerical realization.

Appendix A. Derivation of the numerical fluxes

For the computation of the unsteady solution of the initial value problem (2.22) we use Laplace-transformation as described for example in [4]. We solve Eq. (2.22) separately for $\xi_1 < 0$ and $\xi_1 > 0$ and impose compatibility conditions at $\xi_1 = 0$. We denote the Laplace-transformation of $v(\xi_1, t)$ by $w(\xi_1, s)$:

$$\mathcal{L}\{v(\xi_1,t)\} = w(\xi_1,s). \tag{A.1}$$

The Laplace-transformations of Eq. (2.22) for $\xi_1 > 0 : w^+$ and $\xi_1 < 0 : w^-$ with the corresponding initial conditions read as

$$\frac{\partial^2}{\partial \xi_1^2} w^\pm - \frac{s}{\mu^\pm} w^\pm = -\frac{u^\pm + \xi_1 u^\pm_{\xi_1}}{\mu^\pm}. \tag{A.2}$$

Solutions of the ordinary differential Eq. (A.2) are

$$w^\pm(\xi_1,s) = c_1^\pm \exp\left(-\sqrt{\frac{s}{\mu^\pm}}\xi_1\right) + c_2^\pm \exp\left(\sqrt{\frac{s}{\mu^\pm}}\xi_1\right) + \frac{u^\pm}{s} + \frac{u^\pm_{\xi_1}}{s}\xi_1, \tag{A.3}$$

where $c_1^\pm$ and $c_2^\pm$ are arbitrary constants. As $w^+(\xi_1,s)$ cannot grow exponentially for $\xi_1 \to \infty, c_2^+$ has to be zero. Likewise, c_1^- has to be zero. The other two constants c_1^+ and c_2^- are determined by the conditions

$$\begin{aligned} &w^+(0,s) = w^-(0,s), \\ &\mu^+ \tfrac{\partial w^+}{\partial \xi_1}(0,s) = \mu^- \tfrac{\partial w^-}{\partial \xi_1}(0,s), \end{aligned} \tag{A.4}$$

which establish the spatial continuity of the solution w and the flux $\lambda w_{\xi_1}\xi_1 = 0$. Due to this continuity we restrict ourselves to the function w^+ and get from (A.3)

$$w^+(\xi_1,s) = \frac{-(u^+ - u^-)\sqrt{s\mu^-} + (\mu^+ u^+_{\xi_1} - \mu^- u^-_{\xi_1})}{s\left(\sqrt{s\mu^+} + \sqrt{s\mu^-}\right)} \exp\left(-\sqrt{\frac{s}{\mu^+}}\xi_1\right) + \frac{u^+}{s} + \frac{u^+_{\xi_1}}{s}\xi_1. \tag{A.5}$$

The flux at $\xi_1 = 0$ is then given by

$$f(0,s) = \mu^+ \frac{\partial w^+}{\partial \xi_1}(0,s) = \frac{[\![u]\!]\sqrt{\mu^+\mu^-}}{\sqrt{s}\left(\sqrt{\mu^+} + \sqrt{\mu^-}\right)} + \frac{\sqrt{\mu^+} f^-_{\vec{n}} + \sqrt{\mu^-} f^+_{\vec{n}}}{s\left(\sqrt{\mu^+} + \sqrt{\mu^-}\right)} \tag{A.6}$$

with the trace operator $[\![u]\!] := u^+ - u^-$ and $f^\pm_{\vec{n}} = \mu^\pm u^\pm_{\xi_1}$. The transformation back results in the flux

$$f(0,t) = \mu^+ \frac{\partial w^+}{\partial \xi_1}(0,t) = \frac{[\![u]\!]\sqrt{\mu^+\mu^-}}{\sqrt{\pi t}\left(\sqrt{\mu^+} + \sqrt{\mu^-}\right)} + \frac{\sqrt{\mu^+} f^-_{\vec{n}} + \sqrt{\mu^-} f^+_{\vec{n}}}{\sqrt{\mu^+} + \sqrt{\mu^-}}. \tag{A.7}$$

This flux is singular at $t = 0$, but the time-integral over a finite time step exists as an improper integral. We average it over one time step and use this as numerical flux:

$$g_{\vec{n}} := \frac{1}{\Delta t}\int_0^{\Delta t} f(0,t)\mathrm{d}t = \frac{2[\![u]\!]\sqrt{\mu^+\mu^-}}{\sqrt{\Delta t}\sqrt{\pi}\left(\sqrt{\mu^+} + \sqrt{\mu^-}\right)} + \frac{\sqrt{\mu^+} f^-_{\vec{n}} + \sqrt{\mu^-} f^+_{\vec{n}}}{\sqrt{\mu^+} + \sqrt{\mu^-}}. \tag{A.8}$$

We next describe how to define the *adjoint* flux $g^a_{\vec{n}}$. For this we determine the state u_{S_k} on the interface S_k as given by the solution of the local Riemann problem (2.22) for $t \to 0^+$, which can be computed by a back-transformation of Eq. (A.5) at $\xi_1 = 0$:

$$u_{S_k} = \lim_{t\to 0^+} v(0,t) = \frac{\sqrt{\mu^+}u^+ + \sqrt{\mu^-}u^-}{\sqrt{\mu^+} + \sqrt{\mu^-}}. \tag{A.9}$$

Based on this value and using the rotational invariance we define the numerical flux

$$g^a_{\vec{n}} = (u_{S_k} - u^-)\mu^- \phi^-_{\xi_1}. \tag{A.10}$$

Here, we take the interior value of the diffusion coefficient μ^-, as in the derivation of the weak formulation, this μ belongs to the testfunction.

References

[1] M. Amado, M.J. Tobar, A. Ramil, A. Yez, Application of the Laplace transform dual reciprocity boundary element method in the modelling of laser heat treatments, Eng. Anal. Bound. Elem. 29 (2) (2004) 126–135.

[2] D.N. Arnold, F. Brezzi, B. Cockburn, L.D. Marini, Discontinuous Galerkin methods for elliptic problems, in: B. Cockburn, G. Karniadakis, C.W. Shu (Eds.), Discontinuous Galerkin Methods. Lecture Notes in Computational Science and Engineering, Springer, 2000, pp. 89–101.
[3] D.N. Arnold, F. Brezzi, B. Cockburn, L.D. Marini, Unified analysis of discontinuous Galerkin methods for elliptic problems, SIAM J. Numer. Anal. 39 (5) (2002) 1749–1779.
[4] H. Baehr, K. Stephan, Wärme- und Stoffübertragung, ISBN: 3-54032-334-1, Springer, 2006.
[5] F. Bassi, S. Rebay, Numerical evaluation of two discontinuous Galerkin methods for the compressible Navier–Stokes equations, Int. J. Numer. Methods Fluids 40 (2002) 197–207.
[6] H.S. Carslaw, J.C. Jaeger, Conduction of Heat in Solids, second ed., Oxford Science Publications, Clarendon Press, 1992.
[7] B. Cockburn, G.E. Karniadakis, C.W. Shu, Discontinuous Galerkin methods, Lecture Notes in Computational Science and Engineering, Springer, 2000.
[8] B. Cockburn, C.W. Shu, TVB Runge–Kutta local projection discontinuous Galerkin finite element method for conservation laws II: general framework, Math. Comput. 52 (1989) 411–435.
[9] M. Dumbser, C.-D. Munz, Building blocks for arbitrary high order discontinuous Galerkin schemes, J. Sci. Comput. 27 (2006) 215–230.
[10] G. Gassner, F. Lörcher, C.A. Munz, A contribution to the construction of diffusion fluxes for finite volume and discontinuous Galerkin schemes, J. Comput. Phys. 224 (2) (2007) 1049–1063.
[11] T. Goto, M. Suzuki, A boundary integral equation method for nonlinear heat conduction problems with temperature-dependent material properties, Int. J. Heat Mass Transfer 39 (4) (1996) 823–830.
[12] A. Harten, B. Engquist, S. Osher, S. Chakravarthy, Uniformly high order essentially non-oscillatory schemes III, J. Comput. Phys. 71 (1987) 231–303.
[13] R. Hartmann, P. Houston, Symmetric interior penalty DG methods for the compressible Navier–Stokes equations I: method formulation, Int. J. Numer. Anal. Model. 3 (1) (2006) 1–20.
[14] C. Hirsch, Numerical computation of internal and external flows, Fundamentals of Numerical Discretisation, vol. I, Wiley, 1988.
[15] F. Lörcher, G. Gassner, C.D. Munz, A discontinuous Galerkin scheme based on a space–time expansion I Inviscid compressible flow in one space dimension, J. Sci. Comput. 32 (2) (2007) 175–199.
[16] J.A. Nitsche, Über ein Variationsprinzip zur Lösung von Dirichlet-Problemen bei Verwendung von Teilräumen die keinen Randbedingungen unterworfen sind, Abh. Math. Sem. Univ. Hamburg 36 (1971) 915.
[17] W. Reed, T. Hill, Triangular mesh methods for the neutron transport equation, Technical Report LA-UR-73-479, Los Alamos Scientific Laboratory, 1973.
[18] A. Sutradhar, G.H. Paulino, L.J. Gray, Transient heat conduction in homogeneous and nonhomogeneous materials by the laplace transform Galerkin boundary element method, Eng. Anal. Bound. Elem. 26 (2) (2002) 101–184.
[19] L. van der Tempel, Transient heat conduction in a heat generating layer between two semi-infinite media, J. Heat Transfer 124 (2) (2002) 199–206.